# The last remnants of the Italian Apennine glaciers: 3-D modeling of the Lower Calderone Glacieret by the IDW spatial interpolation of GPR data

Matteo Dossi[1] (ID), Elisabetta Mattei[1] (ID), Massimo Pecci[2,3], Barbara Cosciotti[1] (ID), Sebastian Emanuel Lauro[1] (ID), Angelo Monaco[4], Marco Scozzafava[5] and Elena Pettinelli[1] (ID)

[1]Department of Mathematics and Physics, Roma Tre University, via della Vasca Navale, 84, 00146, Rome, Italy; [2]Department for Regional Affairs and Autonomies, Presidency of the Council of Ministers, via della Stamperia, 8, 00187, Rome, Italy; [3]Italian Glaciological Committee (CGI), corso Massimo D'Azeglio, 42, 10125, Turin, Italy; [4]Studio di Geologia, via Orazio Mattei, 10, 67051, Avezzano, Italy and [5]Mcubo Engineering, via Filippo Corridoni, 11, 67100, L'Aquila, Italy

## Abstract

We present a quantitative ground-penetrating radar (GPR) analysis of the Lower Calderone Glacieret to highlight the recent evolution of one of the southernmost glacial systems in Europe. The Upper and Lower Calderone Glacierets are the last two perennial ice bodies in the Apennine Mountains (Italy), and their continuous monitoring is important for glaciology, hydrology and climate science. We applied a proprietary auto-picking algorithm to track reflections accurately and objectively within three *pseudo*-3-D GPR data sets that were acquired over the Lower Glacieret in different years. After the time-to-depth conversion, the basal reflections were projected onto the normal versors of a 3-D topographic model of the survey area, at the different GPR trace positions. We then applied an Adjusted Inverse-Distance Weighted Spatial Interpolation method to extrapolate the ice-bedrock interface within the areas not directly covered by the GPR profiles and compare it with the topographic surface to recover the glacieret volume. In this paper, we critically examine the accuracy of the reconstructed models, including possible issues related to the challenging survey areas, such as local artifacts in the interpolated interface caused by irregular GPR coverage. We further discuss the various advantages of the implemented procedure with respect to more traditional glacier monitoring techniques.

## 1. Introduction

Glacial environments within mountain regions located at lower latitudes are particularly sensitive to climate change, which can significantly impact the local communities through both direct and indirect processes at different time scales (Richardson and Reynolds, 2000; Kääb and others, 2005). The potential glacial hazards in mountain regions include (a) glacier outburst floods and snow/ice avalanches, which can cause a significant loss of lives, properties and infrastructures within minutes or hours; (b) glacier surges, where rapid increases in the rate of glacier flow can affect large swaths of land in a matter of months or years; and (c) glacier fluctuations, which can disrupt fresh water reservoirs and hydropower generation for decades, especially during severe reduction phases (Richardson and Reynolds, 2000; Kääb and others, 2005). The continuous monitoring of mountain glaciers provides key indicators of the current global climate evolution (Haeberli and others, 2007; Winkler and others, 2010), since the measured annual and seasonal mass balances constitute a direct and undelayed response to local atmospheric conditions (Zemp and others, 2009). The surface mass balance is also one of the main factors that determine the time-lag between climate forcing and the geometrical glacier response (i.e. advance or retreat), together with the glacier slope and elevation range (Zekollari and others, 2020). Further information that can be used in glacier modeling include their internal stratigraphy, total volume, density distribution and Water Equivalent (WE or w.e.; Lundberg and others, 2006; Dossi and others, 2018).

Among the commonly implemented glacier monitoring techniques, direct measurements are generally the most labor-intensive and time-consuming, since they involve networks of manually placed snow probes and ablation stakes, ideally covering the entire glacier surface at regular intervals (Zemp and others, 2009). These probes and stakes are inserted/drilled into the glacier surface, to locally measure the thickness of the superficial snow layer (winter mass balance) and the thickness variation of the deeper firn/ice layers (annual mass balance), respectively. Furthermore, snow pits can also be excavated to directly sample the density of the shallower layers at different depths (Zemp and others, 2009), whereas the deeper and denser firn/ice layers cannot be directly probed without deep-reaching core-sampling drills. In any case, accurate glacier models require a high data density, which may not be feasible for direct measurements when dealing with large survey areas, remote locations or hazardous terrains.

Alternatively, photogrammetric and geodetic techniques are commonly used to create topographic models of an entire glacier surface, by analyzing photographs, satellite images, GPS data sets or LiDAR surveys (Rovelli, 2006; Cogley, 2009; Wang and others, 2014; Rossini and others, 2018). Temporal volumetric changes can thus be obtained by comparing glacier surface models from different periods, with a greater accuracy and higher resolution with respect to direct measurements. However, the estimation of the corresponding mass balance requires these volumetric changes to be combined with accurate density measurements of the surface layers, obtained immediately before the ablation season, although further melting may still occur within the deeper parts of a glacier (Cogley, 2010). Furthermore, these topographic surveys alone cannot be used to recover the total glacier volume at a particular time, unless accurate information is available regarding the glacier bed topography. Nevertheless, estimates of the ice-thickness distribution and the total ice volume can still be obtained from the glacier surface topography, among other inputs, through a method based on the glacier mass turnover and principles of ice-flow mechanics (Farinotti and others, 2009).

More accurate 3-D representations of a glacier can instead be obtained using airborne and ground-based ground-penetrating radar (a.k.a., georadar or GPR) systems (Forte and others, 2014; Dossi and others, 2018). This noninvasive, near-surface, geophysical technique is particularly useful to study glaciological environments, due to the high penetration depth of the electromagnetic (EM) signals within air-ice mixtures, although the presence of liquid water can strongly affect both the EM velocity and the signal attenuation (Bradford and others, 2009; Godio, 2009; Jol, 2009). A GPR system of low enough signal frequency can probe the entire volume of a glacier, while the large number of GPR traces, recorded at high spatial rates ideally over the entire glacier surface, makes the subsequent quantitative analyses statistically sound. In particular, GPR surveys are able to recover the internal stratigraphy along the recorded profiles by combining the reconstructed EM velocity distribution with the arrival times of the identified reflections (Forte and others, 2014; Dossi and others, 2018). The internal density distribution and the WE can also be estimated, under certain conditions and approximations (Forte and others, 2014; Dossi and others, 2018), by using well-known empirical formulas that link the EM velocity with the density of air-ice mixtures (Looyenga, 1965; Robin, 1975; Kovacs and others, 1995; Murray and others, 2007).

The total volume of the glacier can be recovered by using spatial interpolation to extrapolate the basal interface in the areas not directly covered by GPR profiles, and then comparing this interface with the glacier surface topography. The accuracy of the reconstructed interface depends on factors including the basal morphology, the elevation data density, and the interpolation method used (Aguilar and others, 2005; Chaplot and others, 2006). In the presented case study, we apply an Inverse Distance Weighted (IDW) interpolation method (Achilleos, 2011; Rui and others, 2016; Li and others, 2018) to the elevation data obtained from the basal reflections along the various GPR profiles, while additional elevation data from the surrounding topography are further used as boundary constraints.

## 1.1. Historical evolution of the Calderone Glacier

The *Calderone Glacier* was a historical mountain glacier situated within a cirque near the summit of Mt. *Corno Grande* (*Gran Sasso d'Italia* massif), in the Abruzzi Apennines, Italy (Fig. 1a; Giraudi, 2004; Smiraglia and Diolaiuti, 2015). At present, the severely reduced glacial system consists of two glacierets (i.e. small ice bodies with no visible flow pattern; Rau and others, 2005) that extend between 2650 and 2830 m a.s.l. within a deep

depression delimited by the frontal moraine to the North, and two steep ridges to the West and the South–East, which narrow toward the mountain summit (2912 m a.s.l.) to the South–West, reaching the highest point of the Apennine Mountains (Smiraglia and Diolaiuti, 2015; Figure 1a).

The glaciers of the Gran Sasso d'Italia massif reached their maximum extensions during the Last Glacial Maximum (LGM; ~22 600 a BP), before starting to retreat ~21 000 a BP (Giraudi and Frezzotti, 1997). According to estimates, the seasonal snow limit averaged at 1750 m a.s.l. in the massifs of the Central Apennines during the LGM, reaching extremes of 1550 m a.s.l. in the western region and of 1990 m a.s.l. in the eastern region (Federici, 1979; Pecci and D'Aquila, 2011). The Calderone Glacier had five major expansion phases since the start of the Holocene epoch (~11 650 a BP), as observed from both local stratigraphic surveys and the carbon dating of soils interbedded with the deposited glacial till (Giraudi, 2000, 2005). Furthermore, the Holocene glaciation was limited to the Calderone Cirque and the upper section of the underlying *Vallone delle Cornacchie* (i.e. *Deep Valley of the Crows*; Fig. 1a), as inferred from the five known morainic systems (Giraudi, 2000). Nevertheless, the significant steepness of the glacial valley could have either prevented the formation of other potential moraines, or significantly exacerbated their weathering (Giraudi, 2000).

The two older moraines are located at 2350 m a.s.l. (i.e. the *Cornacchie* stage) and 2400 m a.s.l. (i.e. the *Franchetti* stage), respectively to the North-West and West of the nearby *Carlo Franchetti* mountain lodge (2433 m a.s.l.; Fig. 1a; Giraudi, 2000); and they formed some time before 4000 a BP, during temporary reversals of a severe reduction phase (Giraudi, 2004). In fact, the development of a soil layer within the Calderone Cirque between the second and third expansion phases, dated to 3890 ± 60 a BP, indicates a period of extreme reduction of the glacier, if not even its complete disappearance, starting from about 4300 a BP (Giraudi, 2000, 2004).

The three younger moraines (i.e. the *Calderone 1*, *Calderone 2* and *Calderone 3* stages) are found on the northern boundary of the Calderone Cirque (Giraudi, 2000, 2005). The *Calderone 2* system constitutes the main part of the frontal moraine and overlays the *Calderone 1* system, while the *Calderone 3* system to the North-West is further divided into three smaller sections corresponding to three distinct sub-stages (Giraudi, 2000, 2005). In addition, parts of the *Calderone 3* system lack a frontal section and their fallen debris can be found as far down as 2300 m a.s.l., due to a protruding glacier terminus during the Little Ice Age (LIA), when the Calderone Glacier reached its maximum extension of the last 4000 years (Giraudi, 2000).

During the XIX century, the Calderone Glacier did not significantly change from its maximum extension in the LIA (Rovelli, 2006); while a significant serac zone was still active until the end of the century, as inferred from the oldest available photographs from 1871 and 1887, and from morpho-chronological reconstructions (Pecci and D'Aquila, 2011). Nevertheless, after the end of the LIA (~1850), the glacier entered a significant reduction phase that accelerated during the XX century, becoming even more pronounced during the last few decades and continues to the present day. This reduction phase is summarized in Figures 1b, c, as reported in the available literature (Gellatly and others, 1992, 1994; De Sisti and others, 1998; D'Orefice and others, 2000; D'Alessandro and others, 2001; Rovelli, 2006; Pecci and others, 2008; Smiraglia and Diolaiuti, 2015) and inferred from reconstructed models, direct measurements, geodetic studies and geophysical surveys.

The historical models were based on detailed descriptions (Delfico, 1796; Marinelli and Ricci, 1916), paintings and
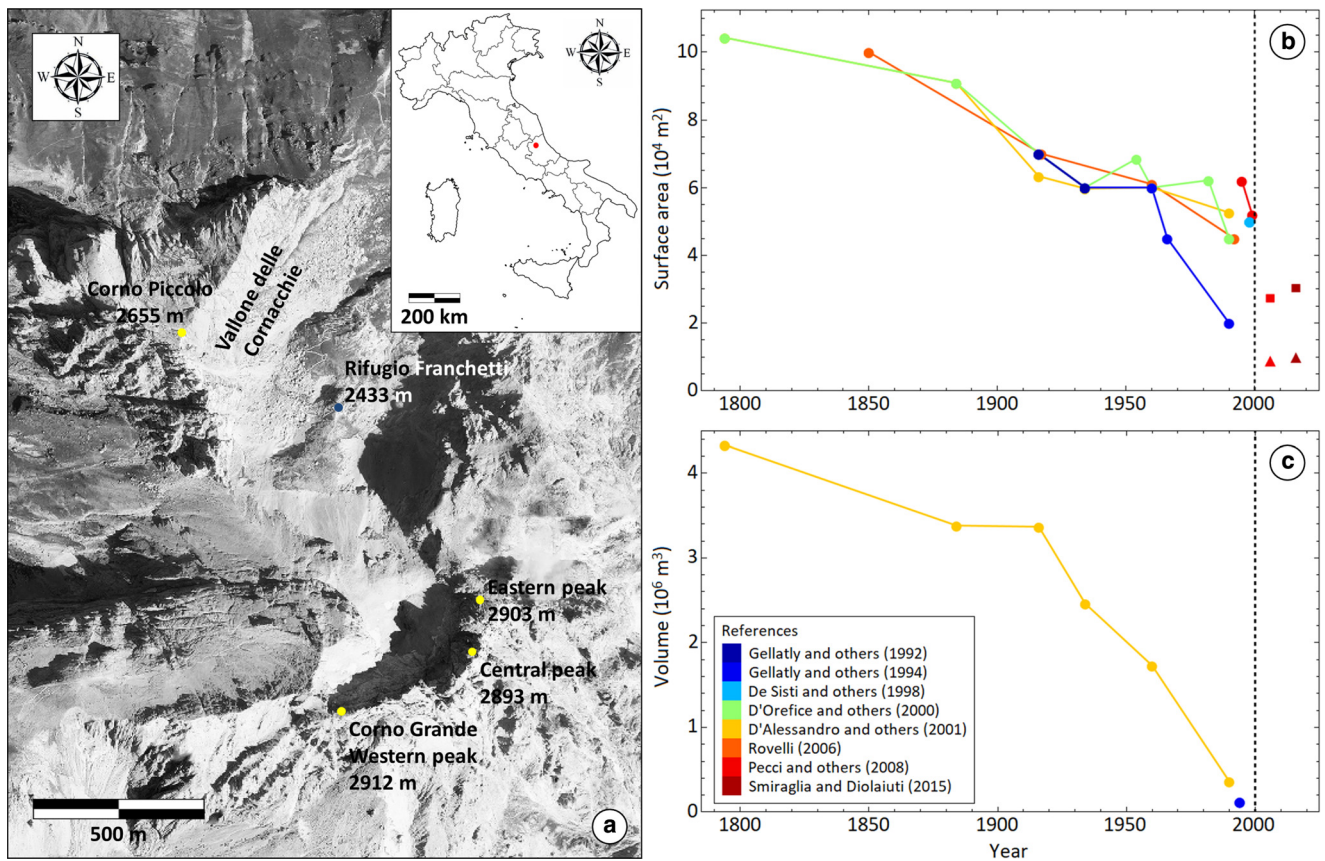
**Figure 1.** Location map and temporal evolution of the Calderone Glacier. The figure shows (a) the position (red dot) of the Gran Sasso d'Italia massif in central Italy, as well as an orthophoto of the Calderone Cirque and of the Vallone delle Cornacchie, with the positions of the Carlo Franchetti mountain lodge (blue dot) and of the main local mountain peaks (yellow dots) superimposed. The orthophoto is courtesy of the Abruzzo Region, and it is obtained from aerial digital photos taken in the 2018–2019 period. The figure also shows both the reconstructed and recorded temporal changes (colored dots) in the surface area (b) and the total volume (c) of the glacier, from the end of the LIA to the present, according to different authors. The vertical dashed line marks the year in which the glacier fragmented into the Lower (colored squares) and Upper (colored triangles) Glacierets. Note that the earliest value reported by Rovelli (2006) in (b) is simply defined as *the maximum extent of the glacier in the XIX century*, and therefore 1850 is used as a stand-in for the unspecified date.

drawings, accurate cartographic records dating between 1884 and 1990, as well as on-site pictures and aerial photos (D'Alessandro and others, 2001; Pecci, 2001; Rovelli, 2006). Between 1794 and

**Table 1.** Historical and recent evolution of the Calderone glacial system between 1920 and 2006, as reported in Pecci and others (2008)

| Period | Cumulative net balance [m w.e.] | Average rate [m w.e. a$^{-1}$] | Greatest annual loss [m w.e.] | Greatest annual gain [m w.e.] |
|---|---|---|---|---|
| CG 1920–94 | −60 | −0.8 | | |
| CG 1995–99 | −1.731 | −0.346 | | |
| LG 2000–06 | −4.208 | −0.601 | −1.746 (2002) | +0.65 (2006) |
| UG 2000–06 | +1.78 | +0.254 | −2.165 (2002) | +2.4 (2006) |
| CE 1920–2006 | −64 | −0.74 | | |
| CE 1995–2006 | −3.841 | −0.32 | | +1.09 (2006) |

The table shows the cumulative net balance and the annual average for different periods, as well as a few notable annual values. After the fragmentation, the Lower Glacieret (LG) showed an almost consistent reduction, with only one other positive annual balance (i.e. +0.263 m w.e. in 2004), while the Upper Glacieret (UG) showed an almost consistent accumulation, with only one negative annual balance (Pecci and others, 2008). After combining the estimates (CE) for the two glacierets with those for the Calderone Glacier (CG), the overall trend from 1995 to 2006 shows an almost consistent reduction, with only one other positive annual balance (i.e. +0.252 m w.e. in 2004; Pecci and others, 2008)

1990, D'Alessandro and others (2001) show the glacier surface area and the total volume respectively decreasing by 49.6 and 91.7% (Figs. 1b, c). Similarly, D'Orefice and others (2000) show the surface area and the average ice thickness decreasing by more than 50% and more than 60% over the same period, respectively, with the reduction significantly accelerating in the second half of the XX century. Conversely, Pecci and others (2008) simulated a considerably more severe reduction (Table 1), by statistically correlating the 1995–2003 mass balances with meteorological data from *Pietracamela* (1000 m a.s.l., ~6 km North from the glacier). The variability in these models underlines the difficulty in accurately reconstructing past glacier evolutions in the absence of repeated and comprehensive field measurements.

## 1.2. Recent surveys and glacier fragmentation

Considering its declining trend, several multidisciplinary studies were conducted in the 1990s to assess the Calderone Glacier as a possible indicator of the effects of human activities, as well as of both regional and global climate changes (D'Alessandro and others, 2001; Pecci, 2001). More recent preliminary surveys aimed at extracting, preserving and studying representative ice cores as part of the *Ice Memory* project, to reconstruct past trends in the global climate more accurately through geochemical analyses (Pavoni and others, 2023). Since 1994, the mass balance of the Calderone Glacier has been measured annually using direct glaciological methods, with surveys respectively conducted at the end of the accumulation (i.e. late May – early June) and

ablation (i.e. late September – early October) seasons (Pecci and others, 2008). Further direct thickness measurements of the accumulated snow are usually performed at the beginning of the ablation season at representative sites, which include the areas in the vicinity of the inserted ablation stakes (Pecci and others, 2008). Such measurements are generally coupled with the excavation of snow pits to locally evaluate the snow density in the shallower layers, and thus infer the corresponding WE (Pecci and others, 2008).

The surface area covered during on-site surveys can sometimes be limited by the steepness of the local topography, as well as the significant risk of rockfalls from the elevated ridges enclosing the cirque (D'Orefice and others, 1995, 2000; Fiucci and others, 1997; De Sisti and others, 1998). In particular, the slope of the glacier surface has been estimated to range between 15° and 30° in the lower section, consistently remain ~30° in the middle section, and steadily increase from 30° to 40° in the upper section (Pecci and others, 2001). In addition, direct measurements became increasingly more difficult over time due to the sustained accumulation of surface debris, in terms of both obtaining accurate readings from the ablation stakes and actually maintaining the network, especially in the lower section (Pecci and others, 2008). On the other hand, several complementary geodetic observations have also been conducted over the years in the middle of both the summer and winter seasons, resulting in a comprehensive photographic archive (Pecci and others, 2008). More than 200 images exist of the Calderone Glacier, just from the period between 1871 and 2005 (Rovelli, 2006), which can thus be cross-referenced with the permanent local geographical features to obtain consistent and accurate geodetic models.

Furthermore, geophysical studies started being performed on the glacier, the earliest examples of which include GPR surveys performed in 1992, 1998 and 1999 (Fiucci and others, 1997; De Sisti and others, 1998; Pecci and others, 2001). During the 1992 survey, the maximum ice thickness of the glacier was estimated at most equal to 26 m, under a debris cover that reached as much as 2 m in thickness in the lower section (Fiucci and others, 1997). The survey also highlighted a clear overdeepening, that is a deep depression in the underlying bedrock caused by previous rapid subglacial erosion (Fiucci and others, 1997). During the 1998 survey, the estimated thickness similarly ranged between 15 and 25 m in the lower section, and between 3 and 6 m in the middle section (De Sisti and others, 1998). During the 1999 GPR survey, the thickness of the lower section ranged between 3 and 27 m, averaging at 15 m, and the upper section reached a maximum thickness of 15 m, while the ice thickness in the middle section tapered down to nothing, thus dividing the glacier ice into two distinct patches (Pecci and others, 2001). Overall, these GPR surveys highlighted a clear reduction in the ice thickness near the terminal moraine, as well as in the central part of the glacier, where rocky outcrops started to appear (Pecci and others, 2001).

By the turn of the century, the glacier was almost completely concealed by a debris layer with a highly variable thickness (e.g. 0.001–1 m in the middle section), which made the identification of its boundaries more difficult in absence of thermal imagery (Shukla and others, 2010; Gök and others, 2023), but also helped maintain the buried ice in the lower section (De Sisti and others, 1998; D'Orefice and others, 2000; Pecci and others, 2001). Nevertheless, the Calderone Glacier eventually fragmented in the summer of 2000 into two smaller ice bodies, thus revealing the glacial sheepback (a.k.a., sheep rock or *roche mountonnée*) landform outcropping in-between them (Pecci and others, 2008; Pecci and D'Aquila, 2011). The upper and lower sections both lack any morphological evidence of glacier dynamics, with the last visible crevasses having been detected in the middle-to-lower section back in 1994, hence the current *glacieret* labels (Rovelli,

2006; Smiraglia and Diolaiuti, 2015). The *Lower Calderone Glacieret* is located at the bottom of the enclosing cirque and is completely buried by a 0.05–1.5 m thick surface layer of rocky debris (Rovelli, 2006); while the *Upper Calderone Glacieret* is located in the uppermost part of the cirque and consists mostly of ice and firn with little debris cover (Pecci and others, 2008). These glacierets are believed to be the last two remaining perennial ice bodies in all of the Apennine Mountains, although a few small multi-year patches of snow can still be found within the mountain range (Smiraglia and Diolaiuti, 2015).

The more recent changes of the Calderone glacial system are summarized in Table 1, and combined with the reconstructed historical changes to highlight the evolution of its reduction phase (Pecci and others, 2008). In particular, the more recent mass balance estimates show a noticeable decrease in the average reduction rate of the glacial system (Table 1), as a result of several factors that contribute to its endurance (Rovelli, 2006), despite the overall reduction trend. In addition to the debris layer covering the Lower Glacieret and its elevated position, both the North-Eastern orientation of the Calderone Cirque and the significant elevation of the enclosing mountain ridges further reduce the exposure of the glacial system to solar radiation, while also leaving it open to the humid North–East winds from the Adriatic Sea (~45 km away; Fig. 1a). Subsequently, the abundant winter precipitations provide both direct and indirect accumulations, with the latter being caused by the frequent snow avalanches from the steep mountain sides (De Sisti and others, 1998; Pecci and others, 2001; Pecci and D'Aquila, 2011; Smiraglia and Diolaiuti, 2015).

In regard to the local climate, the Pietracamela weather station reported on average a slight decrease in the summer temperatures in the ten years after 1995, as well as a slight increase in the total winter snowfalls in the eight years after 1995, when compared to the preceding ten years (Pecci and others, 2008). These trends could help explain the contemporary variability in the annual net balances, in particular the observed outliers of 2004 and 2006 (Table 1), which recorded significant net accumulations (Pecci and others, 2008). In terms of their reported surface area, the Lower and Upper Glacierets slightly increased from 2.7 $10^4$ and 0.9 $10^4$ m$^2$ in 2006 (Pecci and others, 2008), to 3 $10^4$ and $10^4$ m$^2$ in 2011 (Smiraglia and Diolaiuti, 2015), respectively, although possible rounding-related differences should be taken into account. Other potentially distorting factors include the rocky debris cover causing an underestimation of the surface area, and the external residual snow causing an overestimation, with both effects being especially relevant during geodetic surveys. Smiraglia and Diolaiuti (2015) further reported an average thinning rate for the two glacierets equal to about 1 m a$^{-1}$.

## 2. Methods

### 2.1. GPR data acquisition

In this paper, we analyze three *pseudo*-3-D Common Offset (CO) GPR data sets that were acquired during the month of July in 2015, 2016 and 2019, over the Lower Calderone Glacieret (Fig. 2). The applied signal processing was limited to drift (a.k.a., time-zero or zero timing) correction, DC removal and a Butterworth band-pass filter. Even though migration is commonly applied to reconstruct the geometrically correct radar reflectivity distribution within the subsurface, especially regarding dipping reflectors (Jol, 2009), this process was not used for the analysis. In particular, a correct migration analysis would (a) require an accurate EM velocity distribution as input, which is not yet known; (b) need equally spaced traces, which could necessitate the use of a rubber-band interpolation between dedicated marker points, in case of irregular spatial acquisition rates causing
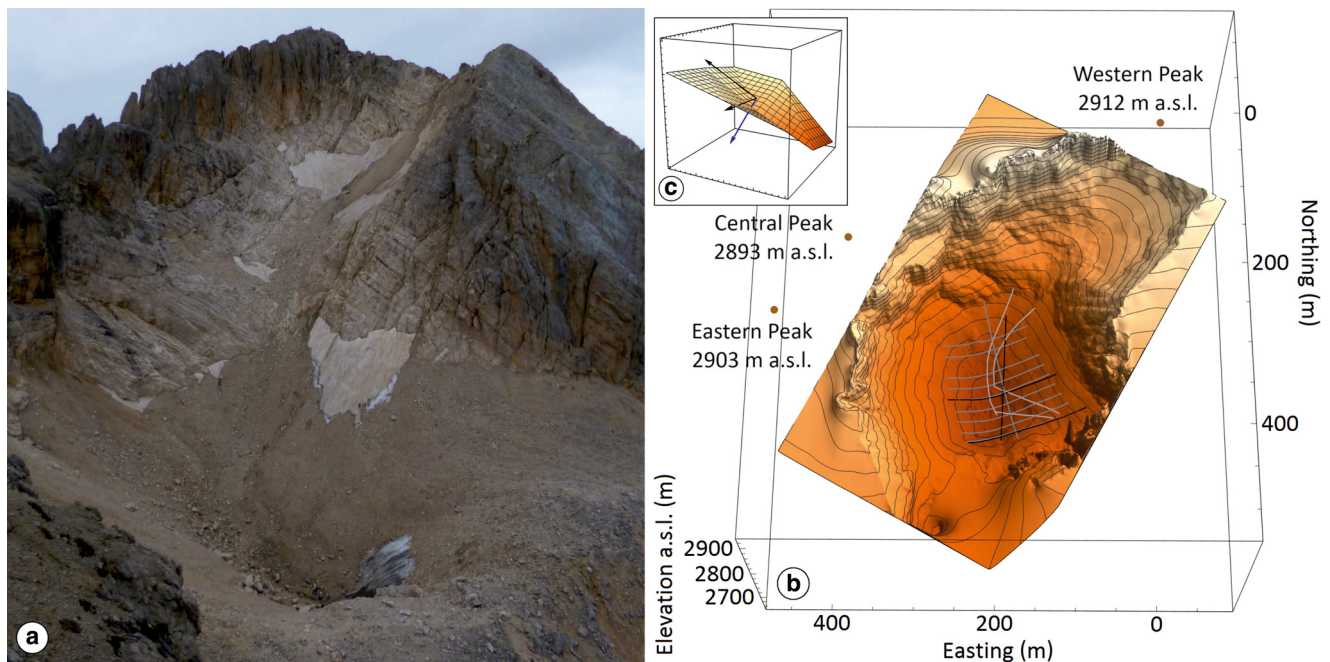
**Figure 2.** Trace positioning over the Lower Calderone Glacieret. The figure shows (a) a view of the Calderone Cirque from a photo taken by Dr Massimo Pecci on 15th September 2016; (b) the 3-D DTM of the Cirque obtained from the 2016 photogrammetric survey, with the contour lines plotted at 10 m elevation intervals, and the GPR survey lines of 2015 (black lines), 2016 (gray lines) and 2019 (light gray lines), superimposed; and (c) the normal versor (blue arrow) of a generic surface, resulting from the vector product of two gradient-based surface versors (black arrows), and used for the 3-D projection of the corresponding GPR trace. For reference, the positions (brown dots) of the nearby mountain peaks (Fig. 1a) are also highlighted in (b), with the mountain summit placed at the origin of both the easting and northing axes.

a stretching of the GPR image in-between such points (Jol, 2009); and (c) potentially negatively impact the recovery of the ice-bedrock interface, which in most of the analyzed data sets is highlighted by interfering diffraction hyperbolas, rather than clear laterally coherent reflections.

The three 2015 CO GPR profiles were acquired using a Zond-12e Radsys GPR system, equipped with 150 MHz air-coupled (hand-held) bistatic unshielded antennas (Monaco and Scozzafava, 2017), with a transmitter–receiver offset of about 2.15 m and an average elevation above the ground-surface of ~20 cm. The same GPR system was later used to acquire the ten 2016 CO GPR profiles, two of which roughly coincide with the transversal profiles of the 2015 dataset (Fig. 2b). In absence of a GPS device during the data acquisition, the various GPR profiles were positioned using fixed reference points whose distance and elevation differences were measured with a Nikon Forestry Pro II Laser Rangefinder-Hypsometer (Monaco and Scozzafava, 2017). In the presented analysis, the GPS coordinates of the western (42°28'10.596"N, 13°33'55.404"E) and eastern (42°28'19.812"N, 13°34'15.024"E) peaks of Mt. Corno Grande (Fig. 1a) were also used as a further constraint for the trace positioning (Fig. 2b).

The four 2019 CO GPR profiles were instead acquired using a PulseEkko Pro GPR system equipped with 250 MHz ground-coupled bistatic Sensors & Software Inc. shielded antennas, with a transmitter-receiver offset equal to 27.94 cm. The various GPR profiles were positioned using specific markers that were accurately recorded at regular intervals along the corresponding survey lines.

A photogrammetric survey (Pecci and others, 2017) was also carried out on 15th September 2016 (i.e. at the end of the ablation season), from which a Digital Terrain Model (DTM) was constructed (Fig. 2b). Considering the initial approximate 13 × 13 cm resolution, the *Point Sampling Tool* plug-in of the *QGIS* open source software was used to discretize the entire surface of the Calderone cirque into a 1 × 1 m grid for the analysis. The

obtained DTM was then used as a reference surface to study the glacieret volume, by comparing it with the basal interfaces constructed over the same grid from each GPR survey. For georeferencing purposes, a few GPS measurements were further acquired at specific reference points on the glacieret surface, such as large boulders (Pecci and others, 2017).

It is important to point out that the use of the same 2016 DTM in all three cases may introduce an additional uncertainty factor, due to potentially significant variations in the surface topography (either local or global) with respect to both 2015 and 2019, that could be caused by changes in both the glacieret volume and the debris cover. Nevertheless, the use of a reference DTM is necessary for a more accurate estimation of the glacieret volume, in absence of a specific DTM for each year, especially considering the highly variable topography of the surveyed area (Pecci and others, 2001).

## 2.2. Time-to-depth conversion

The basal interface of the Lower Glacieret was recovered using an automated reflection strength tracking algorithm designed to track the recorded reflections accurately and objectively along the various GPR profiles (Dossi and others, 2022a). As an example, the horizons marking the main reflections within the longitudinal profiles of the various GPR surveys are highlighted in Figure 3a, showing no significant internal stratigraphy. This lack of internal reflections, combined with the significant presence of surface debris, prevents the implementation of an amplitude inversion algorithm designed to recover the subsurface EM velocity distribution from the identified reflection amplitudes and arrival times (Forte and others, 2014; Dossi and others, 2018).

As an alternative, the hyperbolic diffractions within the various GPR profiles were recovered using an automated diffraction picking algorithm designed to detect subsurface scatterers objectively, track the diffraction phases originating from them accurately, and recover the average subsurface EM velocity above
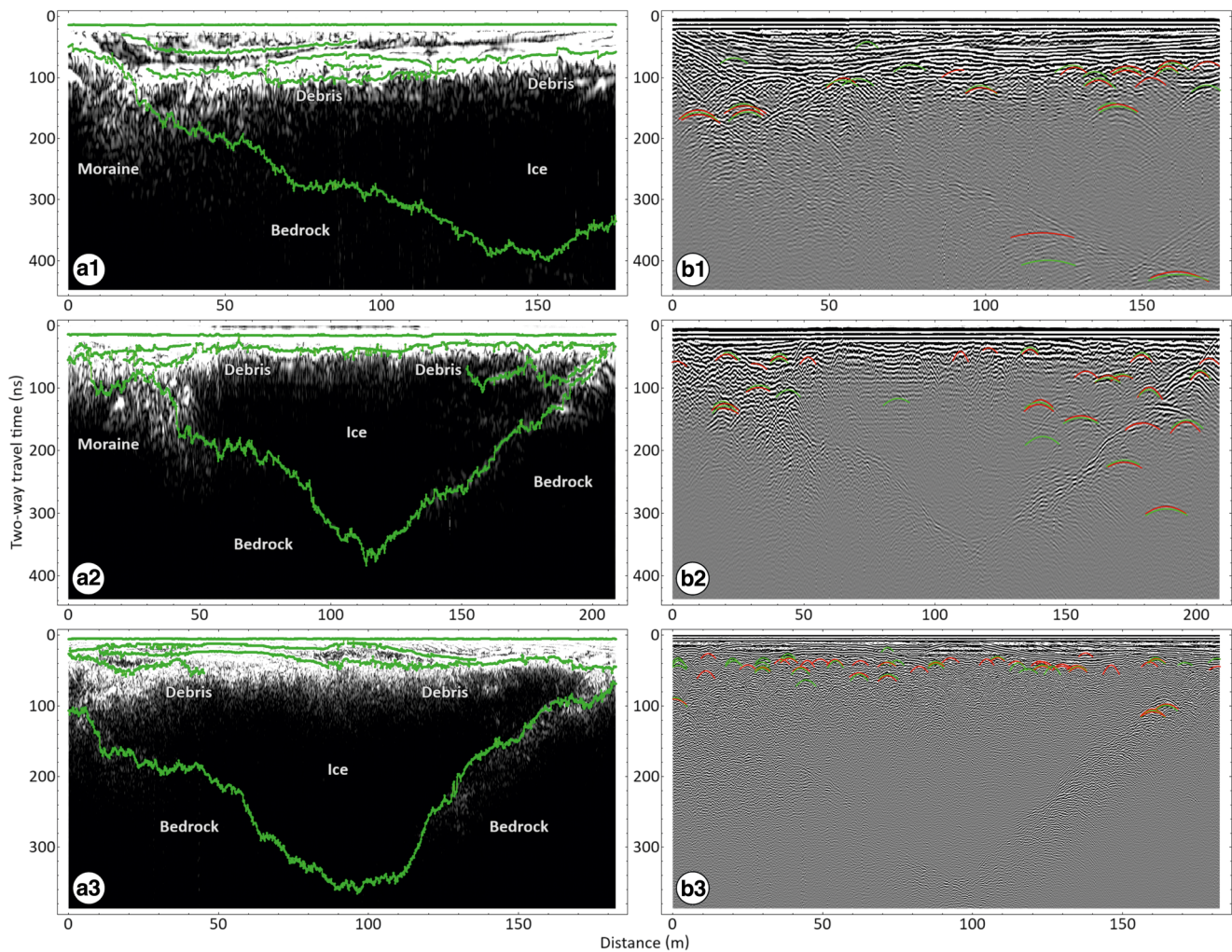
**Figure 3.** Auto-tracking results for the 2015 (first row), 2016 (second row) and 2019 (third row) longitudinal GPR profiles. In each row, the figure shows (a) the auto-tracked horizons (green lines) marking the main recorded reflections, superimposed to the reflection strength profile; and (b) the auto-picked diffraction hyperbolas, superimposed to the corresponding signal amplitude profile, with positive amplitudes marked in green and negative amplitudes marked in red.

each scatterer, among other possible analyses (Dossi and others, 2022b, 2024). The hyperbolas constructed from the aforementioned longitudinal profiles are shown in Figure 3b, and they accurately mark most of the recorded diffractions. As it can be noticed from the results, however, the number of clear undistorted diffractions is limited to a few dozens, which makes the resulting EM velocity model more susceptible to the presence of false positives. In fact, to avoid a significant number of noise-related false negatives, we intentionally did not apply the *automated grouping analysis* in Figure 3b, which disregards isolated false positives by requiring each constructed hyperbola to have at least one other hyperbola of opposite polarity marking another phase of the same diffraction event (Dossi and others, 2022b, 2024).

The shape of the available diffractions can also be affected by (a) the possibly erroneous positioning of the individual GPR traces; (b) the possible presence of out-of-plane diffractions, whose in-plane projections would be placed at the wrong depths; and (c) substantial signal interference, random noise and clutters (Dossi and others, 2022b, 2024). More importantly, the identified diffractions in Figure 3b are mostly concentrated in the shallower section of the glacieret, as in all the other GPR profiles, therefore no significant information regarding the EM velocity within the deeper region can be recovered with this method. As a result of all these issues, it was determined that a statistically sound EM velocity distribution within the Lower Calderone Glacieret could not be recovered from the available GPR data.

For the time-to-depth conversion, we therefore used a reference EM velocity equal to 0.168 m ns$^{-1}$, corresponding to pure ice (Looyenga, 1965), and an associated uncertainty of 10%. The possible glacial systems covered by the considered EM velocities thus range between compact firn at the higher end (Looyenga, 1965; Robin, 1975; Kovacs and others, 1995), and ice containing liquid water for about 2.5–3% of the total volume at the lower end, as estimated from volumetric mixing models (Birchak and others, 1974). The selected uncertainty can also be assumed to cover the irregular 0.05–1.5 m thick surface debris layer (Rovelli, 2006), for which the effect on the total cumulative EM velocity is difficult to be determined locally, with the EM velocity for limestone being equal to 0.12 m ns$^{-1}$ (Davis and Annan, 1989).

In any case, the debris cover will have an overall negligible effect in the calculation of the total thickness, particularly in the deeper areas of the glacieret, when compared to other possible sources of uncertainty, which include (a) possible local deviations from the globally-applied data acquisition and signal processing parameters, such as the utilized trace interval and drift correction; (b) the automatically picked arrival times of the basal reflections, which correspond to the individual peaks of the phase-independent reflection strength in each GPR trace (Fig. 3a; Dossi and others, 2022a), and can be negatively affected by significant noise and interference; (c) the avoidance of migration processes in the applied signal processing, which require accurate EM velocity distributions as input to move dipping

reflectors to their correct positions within GPR profiles (Jol, 2009); and (d) the normal projections of the estimated thicknesses onto the glacieret surface (Fig. 2c; discussed in the following section), which can be affected by local outliers in the DTM (Fig. 2b), as well as erroneous trace positioning.

### 2.3. Digital elevation model of the glacieret base

After the time-to-depth conversion, the tracked basal reflections were projected onto the vertical axes of the individual GPR traces, which were locally estimated from the surrounding topography. In particular, the versor $\hat{n}_{i,j}$ normal to the DTM at a given trace position is calculated through the vector product of the two vectors $\vec{x}_{i,j}$ and $\vec{y}_{i,j}$ (Fig. 2c), which are obtained from the respective components of the local gradient vector of the DTM:

$$\hat{n}_{i,j} = \frac{\vec{x}_{i,j}}{|\vec{x}_{i,j}|} \times \frac{\vec{y}_{i,j}}{|\vec{y}_{i,j}|} \tag{1}$$

with

$$\vec{x}_{i,j} = \left(1, 0, \frac{\text{DTM}_{i,j+1} - \text{DTM}_{i,j-1}}{2\Delta x}\right) \tag{2}$$

$$\vec{y}_{i,j} = \left(0, 1, \frac{\text{DTM}_{i+1,j} - \text{DTM}_{i-1,j}}{2\Delta x}\right) \tag{3}$$

where $(j, i)$ is the closest gridpoint to the considered GPR trace position, and $\Delta x$ is the space interval (i.e. 1 m) used to discretize both the easting and northing positions within the grid. To avoid possible outliers in the calculated normal versors, potentially caused by either isolated artifacts or peculiar small-scale changes in the topography, the gradient vector in each position (whose components are used in Eqns. (2), (3)) was substituted with an average of the local gradient vectors of the DTM (i.e. within a 10 m radius).

After positioning the basal lines within the 3-D model, these were combined with the contour lines of the DTM outside of the glacieret surface (Fig. 2b), to construct a digital elevation model (DEM) of the glacieret base. More specifically, the surrounding contour lines were marked from the DTM at 5 m elevation intervals and used as a boundary condition during the interpolation process, while the extent of the debris-covered glacieret was roughly inferred from the thicknesses estimated at the edges of the various GPR surveys, as well as from the available photographic data. Furthermore, to avoid data redundancy and reduce computational costs, given the high linear density of GPR traces when compared to the grid resolution, the basal lines were re-sampled at 0.5 m elevation intervals using a simple 3-D linear interpolation between adjacent GPR traces.

The elevation of the basal DEM at the various grid positions was calculated using the adjusted IDW spatial interpolation method presented by Li and others (2018). Considering $N_H$ elevation points that belong to either the basal or contour lines, the elevations $h_k$ of these points, and their horizontal distances $d_k$ from the interpolation point located at the $(j, i)$ grid position, the elevation of the DEM at such position is given by the following weighted average (Achilleos, 2011; Rui and others, 2016; Li and others, 2018):

$$\text{DEM}_{i,j} = \frac{\sum_k w_k h_k / d_k^p}{\sum_k w_k / d_k^p} \tag{4}$$

with

$$d_k = \Delta x \sqrt{(i - i_k)^2 + (j - j_k)^2} \tag{5}$$

$$(j, i) \neq (j_k, i_k)$$

$$k = 1, 2, \ldots, N_H$$

$$p = 2$$

where $(j_k, i_k)$ and $w_k$ are respectively the position and adjusting parameter of the $k$-th point of the set; and the exponent $p$ defines the type of interpolation used, namely (assuming all $w_k$ being equal to 1) either a moving average (i.e. $p = 0$), a linear interpolation (i.e. $p = 1$), or a weighted moving average (i.e. $p > 1$). In fact, the higher the value of $p$ is, the smoother the resulting DEM surface becomes (Li and others, 2018).

For the construction of the set of $N_H$ elevation points, we used linear segments branching out of the considered $(j, i)$ grid position at regular angular intervals $\Delta\phi$ (e.g. 15°), to mark the crossed elevation points along the $N_L$ (e.g. 2) closest basal or contour lines to be reached by the segment each time. In addition, after crossing the closest line, each segment is iteratively rotated counterclockwise by $\Delta\phi/N_L$ for each of the remaining $N_L - 1$ lines to be crossed, to avoid the adjusting parameter of the next crossing point to be identically null due to the latter being directly behind the previous point. In particular, the adjusting parameters $w_k$, which may not be commonly applied in IDW interpolations (Achilleos, 2011), are used in Eqn. (4) to reduce the influence of the elevation points further away from the analyzed interpolation point, due to the presence of closer elevation points in-between (Li and others, 2018).

In the calculation of the adjusting parameters, the marked $N_H$ elevation points are re-arranged by increasing values of $d_k$ (Eqn. (5)). As each point effectively casts a shadow onto the points further away, the resulting cumulative effect onto the $k$-th elevation point, caused by some of the $k - 1$ closer points, is based on the relative angular positions of the former with respect to each one of the latter. In particular, the adjusting parameter for the $k$-th elevation point is given by (Li and others, 2018):

$$w_k = \begin{cases} 1 & \text{if} & k = 1 \\ \prod_{m=1}^{k-1} \sin^p[\theta_{k,m}] & \text{if} & k = 2, 3, \ldots, N_H \end{cases} \tag{6}$$

with

$$\theta_{k,m} = \begin{cases} \dfrac{\pi}{2} & \text{if} & \alpha_{k,m} \geq \alpha_{\max} \\ \theta_{k,m} & \text{if} & \alpha_{k,m} < \alpha_{\max} \end{cases} \tag{7}$$

$$\alpha_{\max} = \max\left[\Delta\phi, \frac{2\pi \cdot N_L}{N_H}\right] \tag{8}$$

where $\theta_{k,m}$ is the angle formed by the segment connecting the compared $k$-th and $m$-th elevation points, and the segment connecting the interpolation point with the midpoint of the first segment; $\alpha_{k,m}$ is the angle formed by such elevation points, with the vertex placed on the interpolation point; $\alpha_{\max}$ is the maximum angle for $\alpha_{k,m}$, above which the closer $m$-th point does not cast a shadow onto the $k$-th point further away; and max[...] is an

operator that provides the maximum value among those listed within its argument.

As it can be noticed from Eqn. (7), when the angle $\alpha_{k,m}$ is equal or greater than $\alpha_{max}$, the angle $\theta_{k,m}$ is automatically set equal to $\pi/2$, which in turn sets the corresponding factor in Eqn. (6) equal to 1, thus canceling out the influence of the latter in the calculation of $w_k$. Therefore, the elevation points that have no other point located between them and the interpolation point, will have an uninfluential adjusting parameter $w_k$ (i.e. equal to 1). Notice that the product in Eqn. (6) only considers the elevation points that are closer than the $k$-th point to the interpolation point, while the first elevation point of the set (i.e. $k = 1$) has a value of $w_k$ equal to one (Eqn. (6)), since by construction it has no other elevation point in-between.

Given the potentially large number $N_H$ of elevation points involved in the IDW interpolation at each grid position, the angular step $\Delta\phi$ is used as a minimum value for $\alpha_{max}$ in Eqn. (8), to prevent the latter from becoming uselessly small in Eqn. (7). In addition, the set number $N_L$ of the closest contour or basal lines involved in the analysis is added as a factor in Eqn. (8), as opposed to the formula used in Li and others (2018), since the analyzed elevation points are not randomly distributed, but rather selected through a geometrically determined process. The added factor thus further prevents the resulting angle from becoming too small, and roughly defines the average angular interval within each of the $N_L$ constructed arrays.

## 2.4. Potential DEM artifacts

Common IDW interpolations generally perform better when the sampled elevation points are regularly distributed, while possible artifacts include the *topographic island effect*, by which both hills and basins are turned flat within the innermost circles in topographic maps; and the *bull's eye effect*, by which isolated DEM peaks stick out at the various elevation positions (Achilleos, 2011; Li and others, 2018).

The latter effect is caused by the significantly smaller distance $d_k$ of a given elevation point when the IDW interpolation is performed in its neighborhood, which disproportionally increases the weight of such point by almost turning it into a singularity (Eqn. (4)). The added adjusting parameters $w_k$ (Eqn. (6)) counteract these artifacts by reducing the influence of the points further away while increasing the relative weight of the closer ones (Fig. 4), which likely have elevations similar to the considered point, although the distorting effect may not completely disappear (Li and others, 2018). For instance, the alternation between the constructed basal and contour lines and the void areas in-between caused a slight *stair-stepping effect* (a.k.a., *staircase effect*) that rendered those lines noticeable in the resulting DEMs of the bedrock.

As an example of the shadow effect between two elevation points in the adjusted IDW spatial interpolation, Figure 4 shows the effect of the adjusting parameter $w_2$ of the second point, for 11 different positions with respect to the (closer) first one. In the considered case, Eqn. (4) is simplified into the following equation:

$$\text{DEM}_{i,j} = \frac{(h_1/d_1^2) + ((\sin[\theta_{2,1}])/d_2)^2 h_2}{(1/d_1^2) + ((\sin[\theta_{2,1}])/d_2)^2} \tag{9}$$

The effects of the shadow cast by the first elevation point onto the second one are visible in Figure 4d at the positions 3–8 of the second point. Most notably, an abrupt change in the interpolated elevation can be noticed between the positions 8 and 9 (Fig. 4d), caused by the angle $\alpha_{2,1}$ surpassing the threshold $\alpha_{max}$ (Fig. 4c),

while the asymmetry in the graphs is mainly caused by the increasing distance $d_2$ (Fig. 4a).

## 3. Results

The construction process of the basal DEMs of the Lower Calderone Glacieret is presented in Figure 5, for the different GPR surveys. As it can be noticed, the utilized basal and contour lines tend to not be as regularly distributed along the analyzed grid as they would be expected in the ideal case (Li and others, 2018). This is most prominently the case for the 2015 (Fig. 5a-1) and 2019 (Fig. 5a-3) data, where large gaps can be observed between the basal and contour lines, in the areas not covered by the GPR surveys. Irregular distributions can also be observed in the 2016 dataset (Fig. 5a-2), namely at the abrupt transitions between the transversal basal lines and the longitudinally oriented contour lines, as well as at the relatively smaller gaps in the steeper southern section of the glacieret. The artifacts originating from such data arrays can be noticed in the constructed basal DEMs (Fig. 5b), although they ultimately affect the resulting 3-D models at very different degrees.

In the 2015 DEM, the IDW interpolation replaced the large gaps generally with inward bumps (Fig. 5b-1), as opposed to the expected basin, mainly due to the larger influence of the elevated and relatively closer contour lines (Fig. 5a-1). Similar deformations can also be noticed on the left side of the 2019 DEM, while on the right side the reconstructed interface shows an unrealistically smooth surface in the transition between the contour and basal lines (Fig. 5b-3). Apart from a preemptively higher data density over the surveyed area, a theoretical post-acquisition solution for these kinds of artifacts could be an increase in the number of elevation points marked along the basal lines for the IDW interpolation, with respect to those in the contour lines, albeit with a subsequent increase in the computational cost. Alternatively, the weights of the basal lines could be purposefully increased in the calculation of the DEM, either subjectively or based on a specified radiation pattern. In the case of the 2015 and 2019 data sets, we attempted to obtain more realistic basal DEMs by applying an elliptical IDW method (Merwade and others, 2006), which would have better accounted for the directional morphology of the glacieret base. In particular, at each interpolation point (e.g. blue dots in Fig. 5a) the weights of the various elevation points used in the calculation (i.e. brown dots in Fig. 5a) were modified by projecting the corresponding distances (Eqn. (5)) onto ellipsoidal surfaces that were iteratively fitted to the different sets of elevation points (Ying and others, 2012). However, these attempts were ultimately abandoned, since the resulting changes were deemed to be negligible within the gaps, while also being excessively distorting in the more densely sampled areas.

The 2016 DEM can be considered acceptable for further analyses of the surface area and volume of the Lower Calderone Glacieret, although some tongue-shaped artifacts can still be noticed, especially on the left side of the survey area (Fig. 5b-2). These can be attributed to both the aforementioned abrupt transitions between the basal and contour lines, and possible trace positioning errors that, for instance, could cause a given transversal GPR profile to be locally shifted with respect to the two adjacent ones. Nevertheless, useful information can still be recovered from the reconstructed basal topography model (Fig. 6a), which also includes the *upper* and *lower uncertainty DEMs* (Fig. 6b). The latter were constructed by applying the same IDW interpolation process used for the *reference basal DEM* (Fig. 5a-2), however the EM velocities used for the time-to-depth conversion (which defines the basal lines) are respectively equal to the lower and upper ends of the previously discussed ±10% range.
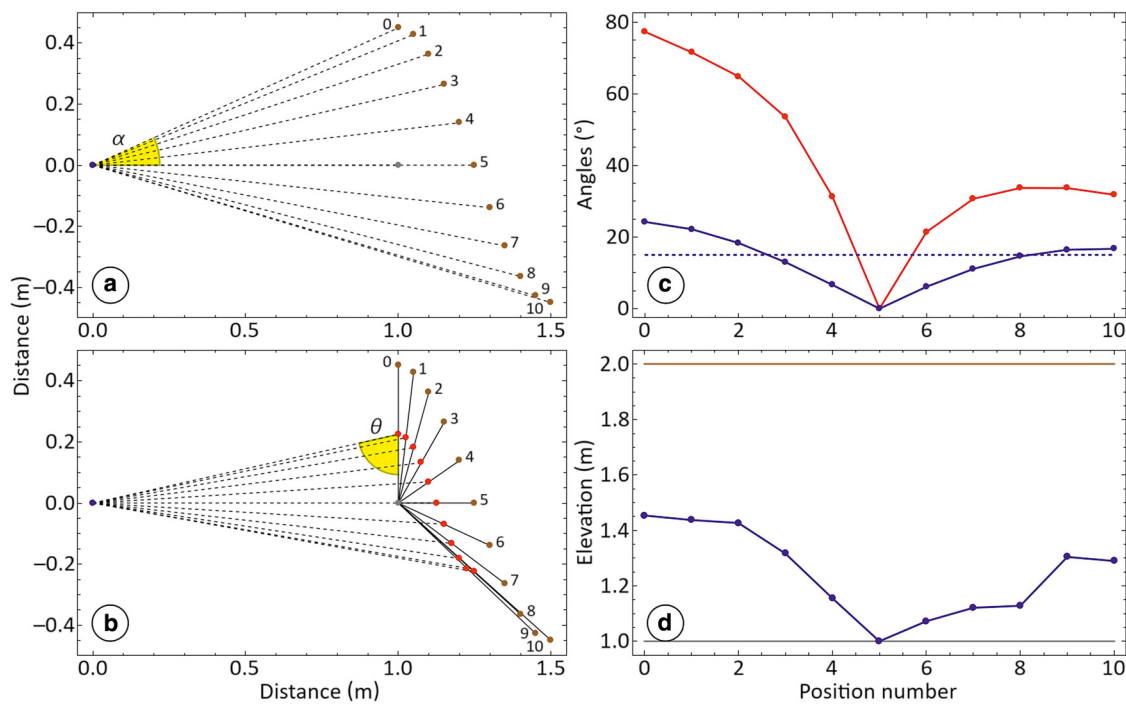
**Figure 4.** Exemplary shadow effect between two elevation points, used to prevent bull's eye artifacts during the IDW spatial interpolation. The figure shows (a) the interpolation point (blue dot), the first elevation point (gray dot), and the different (numbered) positions of the second point (brown dots), with the segments (dashed lines) separately connecting the interpolation point with the elevation points in the various cases, and with the angle $\alpha_{2,1}$ (Eqn. (8)) at the first position highlighted (yellow sector); and (b) the same geometry as in (a), with one set of segments (solid lines) connecting the two elevation points (gray and brown dots) in the different cases, and the other (dashed lines) connecting the interpolation point (blue dot) to the midpoints (red dots) of the former in said cases, and with the angle $\theta_{2,1}$ (Eqns. (7), (9)) at the first position highlighted (yellow sector). The figure also shows (c) the angles $\alpha_{2,1}$ (blue dots) and $\theta_{2,1}$ (red dots) formed in the various cases by the segments in (a) and (b), as well as the maximum value $\alpha_{max}$ (dashed line), set equal to 15° in this example; and (d) the elevation (blue dots) extrapolated in the interpolation point in the different geometries, compared to the constant elevations for the first (gray line) and second (brown line) points, chosen as an example.

The surface area of the glacieret was obtained from the null-thickness contour line (Fig. 6a) of the difference between the surface DTM (Fig. 2b) and the basal 2016 DEM (Fig. 5b-2). The identified surface area is equal to $2.37 \ 10^4 \, \mathrm{m}^2$ on the horizontal plane, while it is equal to $2.71 \ 10^4 \, \mathrm{m}^2$ when the local topography is taken into account, with the glacieret surface being approximated as planar between each triplet of adjacent points forming a right triangle within the grid (Fig. 2c). These approximated estimates are comparable with both the $2.7 \ 10^4 \, \mathrm{m}^2$ estimated by Pecci and others (2008) for 2006, and the possibly rounded-up $3 \ 10^4 \, \mathrm{m}^2$ reported by Smiraglia and Diolaiuti (2015) for 2011 (Fig. 1b). In terms of volume estimates, the average vertical thickness (i.e. DTM-DEM difference) calculated within the horizontal area is equal to $13.3 \pm 1.5 \, \mathrm{m}$, where the associated uncertainty is given by the average differences between the reference basal DEM and the upper and lower DEMs (Fig. 6b). Consequently, the total volume of the Lower Calderone Glacieret in 2016 is calculated as $3.15 \ 10^5 \pm 0.35 \ 10^5 \, \mathrm{m}^3$, which is comparable with the $3.61 \ 10^5 \, \mathrm{m}^3$ estimated by D'Alessandro and others (2001) for 1990 (Fig. 1c), and almost three times the $1.2 \ 10^5 \, \mathrm{m}^3$ roughly estimated by Gellatly and others (1994). Notice that both historical estimates include the upper section of the then still whole Calderone Glacier, while the high variability in the estimated glacieret volumes highlights the difficulty in accurately reconstructing its basal interface. In fact, considering the significantly reduced size of the glacieret, the irregularity of the basal topography constitutes an ever more influential uncertainty factor in the estimation of the total glacieret volume.

This is particularly evident when considering the volume-area scaling (VAS) empirical relations, which are widely applied in glacier inventories and water resource estimations, and are based on data from large populations of studied glaciers (Bahr and others, 2015; Colucci and Žebre, 2016). As an example, two functions that have been used to estimate the volume of glaciers and glacierets from their surface areas, are given by (Bahr and others, 2015; Colucci and Žebre, 2016):

$$V = 0.03 \cdot S^{1.36} \quad \text{with} \quad 0.1 \, \mathrm{km}^2 < S < 1000 \, \mathrm{km}^2 \tag{10}$$

$$V = 0.0329 \cdot S^{1.1509} \quad \text{with} \quad 0.01 \, \mathrm{km}^2 < S < 1.0 \, \mathrm{km}^2 \tag{11}$$

where $V$ and $S$ are respectively the volume (in $\mathrm{km}^3$) and the surface area (in $\mathrm{km}^2$) of the considered glacial bodies.

Since volume-area relationships might fail for glacier sizes that fall outside the range of the observed data (Bahr and others, 2015), Eqn. (11) was proposed by Colucci and Žebre (2016) specifically for small and very small glaciers and glacierets, down to ice patches covering just $10^4 \, \mathrm{m}^2$, in order to reconstruct the evolution of glaciers in the southeastern Alps during the Late Holocene. Although the sizes of the Upper and Lower Calderone Glacierets (Fig. 1b) fall within the acceptable range for Eqn. (11), as this relation defines an average trend within the considered statistical population, the accuracy of the resulting estimates might not be considered acceptable for further quantitative analyses (e.g. WE estimation). For instance, while the estimated $2.71 \ 10^4 \, \mathrm{m}^2$ topographic surface area and the $3.15 \ 10^5 \pm 0.35 \ 10^5 \, \mathrm{m}^3$ total glacieret volume are comparable with the fitted glaciological data (Colucci and Žebre, 2016), the Lower Glacieret volume obtained from Eqn. (11) would be equal to $5.17 \ 10^5 \, \mathrm{m}^3$, which is about 64.1% higher than the estimated $3.15 \ 10^5 \, \mathrm{m}^3$ mean volume.
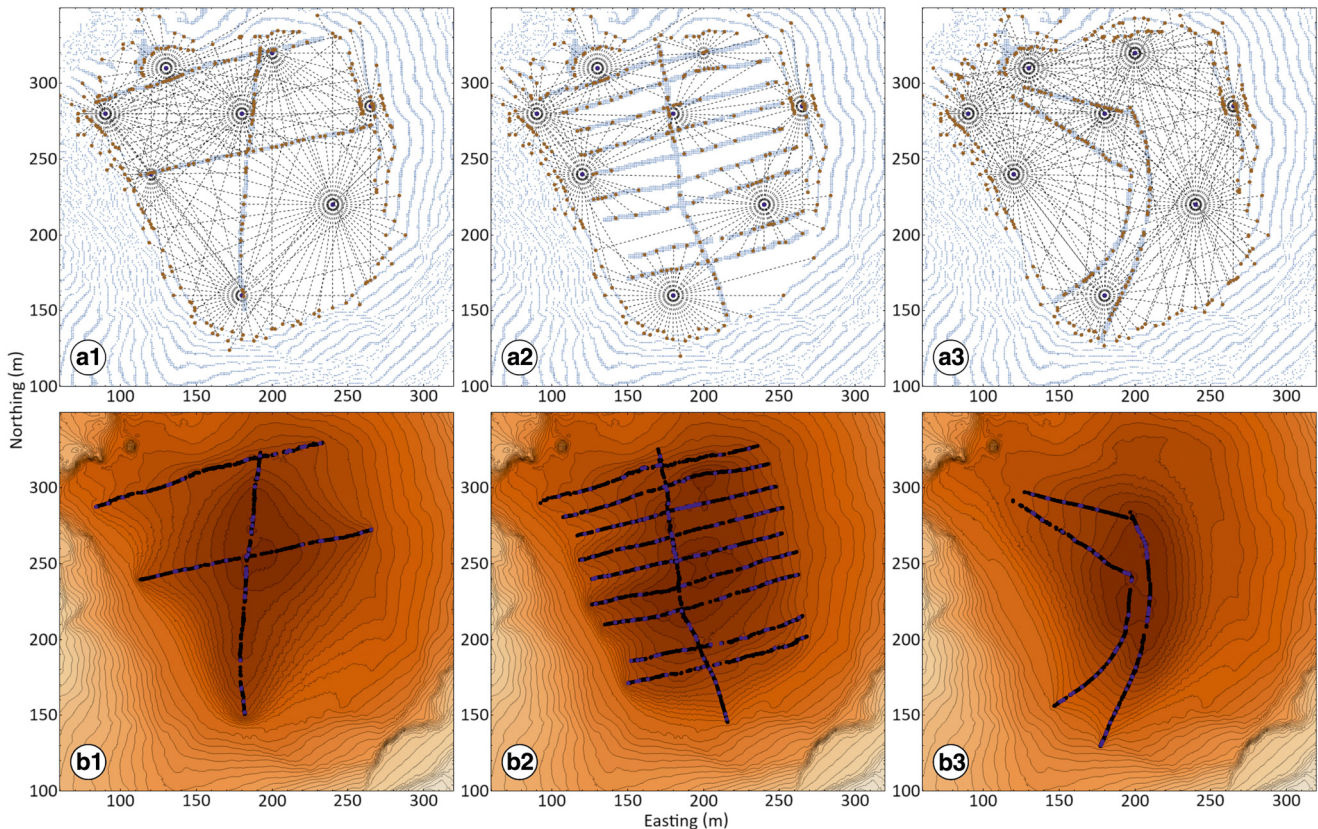
**Figure 5.** Construction of the basal DEMs of the Lower Calderone Glacieret from the 2015 (first column), 2016 (second column) and 2019 (third column) GPR surveys. In each column, the figure shows (a) the utilized basal and contour lines (blue pixels), and the horizontal distances (dashed lines) between the elevation (brown dots) and interpolation (blue dots) points used in the calculation of the DEM at eight exemplary locations (Eqn. (4)); and (b) the contour plot of the resulting DEM, with superimposed the basal lines (black dots) obtained from the GPR profiles and re-sampled at 0.5 m elevation intervals. For visual clarity, the blue dots in (b) highlight bed elevations equal to the corresponding plotted contour lines, which mark 5 m elevation intervals, similarly to the topographic contour lines in (a).

## 4. Discussion

Irrespective of the morphology and surface area, the dependence of the reconstructed DEM on the particular spatial interpolation method used is observed to decrease with increasing elevation data density (Chaplot and others, 2006). More specifically, Chaplot and others (2006) report few differences between the techniques studied, provided that the sampling density was high, simply due to the decrease of the average distance between the known values. Similarly, Aguilar and others (2005) concluded that the factor that has the greatest influence on the quality of the surface interpolated from scattered data was the landscape morphology, followed by the sampling density, and then by the applied interpolation method.

Regarding the reconstructed DEMs, the difficulty in obtaining accurate volume estimates can also be noticed when observing the negative thicknesses obtained in areas not covered by their respective GPR surveys. In the 2016 model, these artifacts are located outside of the identified glacieret boundaries (Figs. 6a, b), due to the basal DEM being slightly higher than the surface DTM in some areas; and they can be expected for the surrounding topography, where the interpolated DEM and the recorded DTM are supposed to coincide. On the other hand, these artifacts have a much more substantial presence in the 2015 (Fig. 6c) and 2019 (Fig. 6d) models, even within the 2016 boundaries, due to the more limited areas covered by the GPR profiles. In particular, the straightforward IDW interpolation connecting the basal and contour lines over the aforementioned gaps (Figs. 5a-1, a-3) caused the resulting DEMs (Figs. 5b-1, b-3) to have an elevation that is significantly higher than the DTM of the glacieret surface. Therefore, it is ultimately not

possible to estimate the volume of the Lower Calderone Glacieret accurately and objectively from the 2015 and 2019 models, which would have allowed to examine its recent evolution together with the 2016 model. Another possible method to obtain these volume estimates would have been to compare the basal DEM from 2016 with surface DTM from the other years, however such data are not available for the presented analysis.

Nevertheless, it is still possible to compare the thicknesses of the different models along their respective basal lines, with the resulting average values for the 2015, 2016 and 2019 surveys being respectively equal to 16.1, 14.6 and 15.4 m. As it can be noticed, the 2016 average thickness calculated along the basal lines is just within the upper limit of the uncertainty interval of the value obtained over the entire surface of the glacieret model (i.e. $13.3 \pm 1.5$ m), which highlights the importance of a 3-D analysis for accurate volume estimates, compared to a 2-D one. In any case, as the 2016 3-D glacieret model is the only one available, a more direct comparison between the surveys would theoretically be to analyze the thicknesses along the same paths within such model, which results in the aforementioned average values being respectively equal to 12.5, 14.6 and 15.3 m. However, this comparison is not valid due to the previously discussed trace positioning issues, which can lead to significant discrepancies within those areas that are not covered by all surveys, since such areas rely more heavily on the accuracy of the IDW interpolation. An additional uncertainty factor is the use of the same 2016 DTM in all three cases (Fig. 2b), with DTMs from the other years not being available. Therefore, the analysis does not take into account possible temporal changes in the surface topography, whether locally or globally, with respect to both 2015 and 2019.
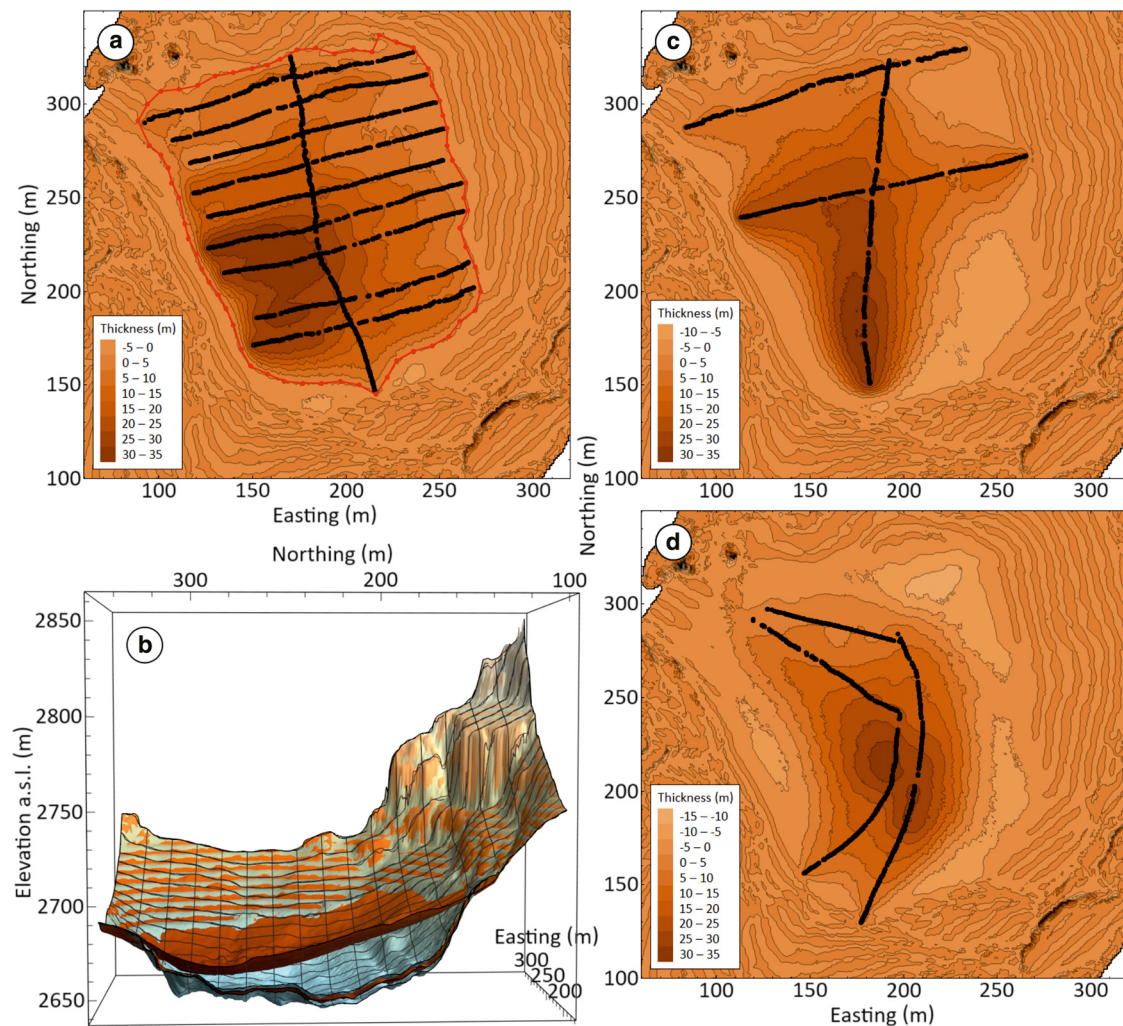
**Figure 6.** Thickness of the Lower Calderone Glacieret, as inferred from the various models. The figure shows (a) the difference in elevation between the DTM (Fig. 2b) of the glacieret surface and the 2016 DEM (Fig. 5b-2) of the glacieret base, with the obtained surface boundary (red line) following the null-thickness contour line; and (b) a cross section of the 2016 DTM and DEM (sienna tones), that includes the upper and lower DEMs (silver tones), which highlight the uncertainty of the reconstructed basal interface. For completeness, the figure also shows the difference between the DTM and the reconstructed 2015 (c) and 2019 (d) basal DEMs (Figs. 5b-1, b-3), in which artificial negative thicknesses can be observed in the large areas not covered by the respective GPR surveys.

Nevertheless, the most noticeable differences in the thickness of the different models along the basal lines can be observed at the edges of such lines (Fig. 6). In particular, the large differences between the 2016 and 2019 models are mainly responsible for the potentially misleading increase in the calculated average thickness from 14.6 to 15.4 m. More specifically, the higher thicknesses obtained at the southern end of the 2019 survey (Fig. 6d) would indicate a deeper basal interface with respect to the 2016 model (Fig. 6a) over the same area. Notwithstanding possible temporal changes in the local topography, these discrepancies can be attributed to a local lack of data within the 2016 dataset, thus highlighting another uncertainty factor that can be expected from spatially limited GPR surveys.

## 5. Conclusion

We presented a quantitative GPR analysis in which we constructed and compared the basal DEMs of the Lower Calderone Glacieret for 2015, 2016 and 2019; while also discussing both the advantages and limitations of the implemented procedure. We highlighted the need for GPR surveys that cover the entire surface of a glacier at regular intervals, as well as for accurate internal EM velocity distributions for the time-to-depth conversion, to estimate of the total volume as accurately as possible.

This issue is especially relevant for small glaciers and glacierets, in which peculiar topographical anomalies constitute a significant uncertainty factor compared to the smaller sizes of these ice bodies.

In the case of the Lower Calderone Glacieret, the lack of a clearly identifiable internal stratigraphy, combined with the significant surface debris cover, and the localization of the small number of usable undistorted diffractions within the shallower sections, prevented the reconstruction of the internal EM velocity distribution by means of either amplitude inversion or diffraction analysis. We therefore used a reference EM velocity equal to 0.168 m ns$^{-1}$, with an associated uncertainty of ±10%, for the time-to-depth conversion. In regard to the recent temporal changes, the low data densities of the 2015 and 2019 GPR surveys ultimately prevented a direct comparison between the various glacieret models in terms of the resulting volumes. However, a 2-D analysis of the individual GPR profiles still suggests a general decrease in the average glacieret thickness over time.

The reconstructed glacieret model for 2016 allowed us to calculate a topographic surface area of 2.71 $10^4$ m$^2$ and a total volume of 3.15 $10^5$ ± 0.35 $10^5$ m$^3$. Both values are consistent with the more recent estimates from literature, although the logistical difficulties in surveying the steeper upper section of the glacieret could have caused a slight underestimation. In conclusion,

considering the challenging terrain, the presented case study demonstrated the advantages of GPR surveys with respect to more traditional glacier monitoring techniques. In particular, its ability to probe the entire volume of the debris-covered glacieret at high data densities significantly improved the validity of the reconstructed 3-D model.

## References

Achilleos GA (2011) The inverse distance weighted interpolation method and error propagation mechanism – creating a DEM from an analogue topographical map. *Journal of Spatial Science* **56**(2), 283–304. doi: 10.1080/14498596.2011.623348

Aguilar FJ, Agüera F, Aguilar MA and Carvajal F (2005) Effects of terrain morphology, sampling density, and interpolation methods on grid DEM accuracy. *Photogrammetric Engineering and Remote Sensing* **71**(7), 805–816. doi: 10.14358/PERS.71.7.805

Bahr DB, Pfeffer WT and Kaser G (2015) A review of volume-area scaling of glaciers. *Reviews of Geophysics* **53**(1), 95–140. doi: 10.1002/2014RG000470

Birchak JR, Gardner CG, Hipp JE and Victor JM (1974) High dielectric constant microwave probes for sensing soil moisture. *Proceedings of the IEEE* **62**(1), 93–98. doi: 10.1109/PROC.1974.9388

Bradford JH, Nichols J, Mikesell TD and Harper JT (2009) Continuous profiles of electromagnetic wave velocity and water content in glaciers: an example from Bench Glacier, Alaska, USA. *Annals of Glaciology* **50**(51), 1–9. doi: 10.3189/172756409789097540

Chaplot V and 5 others (2006) Accuracy of interpolation techniques for the derivation of digital elevation models in relation to landform types and data density. *Geomorph* **77**(1–2), 126–141. doi: 10.1016/j.geomorph.2005.12.010

Cogley JG (2009) Geodetic and direct mass-balance measurements: comparison and joint analysis. *Annals of Glaciology* **50**(50), 96–100. doi: 10.3189/172756409787769744

Cogley JG (2010) Mass-balance terms revisited. *Journal of Glaciology* **56**(200), 997–1001. doi: 10.3189/002214311796406040

Colucci RR and Žebre M (2016) Late Holocene evolution of glaciers in the southeastern Alps. *Journal of Maps* **12**(S1), 289–299. doi: 10.1080/17445647.2016.1203216

D'Alessandro L, D'Orefice M, Pecci M, Smiraglia C and Ventura R (2001) The strong reduction phase of the Calderone glacier during the last two centuries: reconstruction of the variation and of the possible scenarios with GIS technologies. In Visconti G, Beniston M, Iannorelli ED and Barba D (eds), *Advances in Global Change Research*, Vol. **9**. Dordrecht, Netherlands: Kluwer Acad. Publ., pp. 425–433.

Davis JL and Annan AP (1989) Ground-penetrating radar for high resolution mapping of soil and rock stratigraphy. *Geophysical Prospecting* **37**(5), 531–551. doi: 10.1111/j.1365-2478.1989.tb02221.x

Delfico O (1796) *Osservazioni di Orazio Delfico su di una piccola parte degli Appennini dirette a sua eccellenza il Signor Marchese D. F. Mazzocchi, Presidente del Sacro Regio Consiglio*. L'Aquila, Italy: Bibl. Prov.

De Sisti G, Marino A and Pecci M (1998) Indagini georadar sul Ghiacciaio del Calderone del Gran Sasso d'Italia: Primi dati relativi alla ricostruzione dello spessore del ghiaccio residuo. Proc. 17th Conf. GNGTS, Rome, Italy, 10–12 November 1998, 1–6.

D'Orefice M, Ledonne L, Pecci M, Smiraglia C and Ventura R (1995) Nuovi dati sull'alimentazione nevosa del Ghiacciaio del Calderone (Gran Sasso d'Italia, Appennino Centrale). *Geografia Fisica e Dinamica Quaternaria* **18**, 253–256.

D'Orefice M, Pecci M, Smiraglia C and Ventura R (2000) Retreat of Mediterranean glaciers since the Little Ice Age: case study of Ghiacciaio del Calderone, Central Apennines, Italy. *Appellate Authority for Advance Ruling* **32**(2), 197–201. doi: 10.1080/15230430.2000.12003355

Dossi M, Forte E, Pipan M and Colucci RR (2018) Quantitative 3-D GPR analysis to estimate the total volume and water content of a glacier. Proc. IEEE 17th Int. Conf. GPR, Rapperswil, Switzerland, 18–21 June 2018, 1–6, doi: 10.1109/ICGPR.2018.8441636

Dossi M and 6 others (2022a) Automated reflection strength tracking for improved stratigraphic interpretation of GPR data sets. Proc. SEG 19th Int. Conf. GPR, Golden, Colorado, USA, 12–17 June 2022, 123–126, doi: 10.1190/gpr2022-016.1

Dossi M and 6 others (2022b) Automated detection and tracking of hyperbolic diffractions applied to engineering GPR data sets. Proc. SEG 19th Int. Conf. GPR, Golden, Colorado, USA, 12–17 June 2022, 127–130, doi: 10.1190/gpr2022-017.1

Dossi M and 6 others (2024) Estimation of the subsurface electromagnetic velocity distribution from diffraction hyperbolas by means of a novel automated picking procedure: theory and application to glaciological ground-penetrating radar data sets. *Geophysics* **89**(2), KS53–KS68. doi: 10.1190/geo2023-0042.1

Farinotti D, Huss M, Bauder A, Funk M and Truffer M (2009) A method to estimate the ice volume and ice-thickness distribution of alpine glaciers. *Journal of Glaciology* **55**(191), 422–430. doi: 10.3189/002214309788816759

Federici PR (1979) Una ipotesi di cronologia glaciale Würmiana, tardo e post-Würmiana nell'Appennino Centrale. *Geografia Fisica e Dinamica Quaternaria* **2**, 196–202.

Fiucci A, Gigante B, Rossi C, Smiraglia C and Veggetti O (1997) The Calderone Glacier (Gran Sasso d'Italia). Determination of ice thickness and bedrock morphology by means of Radio-Echo Sounding. *Geografia Fisica e Dinamica Quaternaria* **20**, 305–308.

Forte E, Dossi M, Pipan M and Colucci RR (2014) Velocity analysis from common offset GPR data inversion: theory and application to synthetic and real data. *Geophysical Journal International* **197**(3), 1471–1483. doi: 10.1093/gji/ggu103

Gellatly AF, Grove JM and Smiraglia C (1992) Alcuni risultati di recenti ricerche sul Ghiacciaio del Calderone (Gran Sasso d'Italia, Abruzzo). *Geografia Fisica e Dinamica Quaternaria* **15**, 111–113.

Gellatly AF, Smiraglia C, Grove JM and Latham R (1994) Recent variations of Ghiacciaio del Calderone, Abruzzi, Italy. *Journal of Glaciology* **40**(136), 486–490. doi: 10.3189/S0022143000012351

Giraudi C (2000) Le oscillazioni oloceniche del Ghiacciaio del Calderone Gran Sasso d'Italia (Abruzzo - Italia). *Ital. J. Quat. Sci* **13**(1-2), 31–36.

Giraudi C (2004) The Apennine glaciations in Italy. In Ehlers J and Gibbard PL (eds), *Quaternary Glaciations - Extent and Chronology - Part 1: Europe*. Amsterdam, Netherlands: Elsevier B.V., pp. 215–223.

Giraudi C (2005) Middle to Late Holocene glacial variations, periglacial processes and alluvial sedimentation on the higher Apennine massifs (Italy). *Quaternary Research* **64**(2), 176–184. doi: 10.1016/j.yqres.2005.06.007

Giraudi C and Frezzotti M (1997) Late Pleistocene glacial events in the Central Apennines, Italy. *Quaternary Research* **48**(3), 280–290. doi: 10.1006/qres.1997.1928

Godio A (2009) Georadar measurements for the snow cover density. *American Journal of Applied Sciences* **6**(3), 414–423. doi: 10.3844/ajassp.2009.414.423

Gök DT, Scherler D and Anderson LS (2023) High-resolution debris-cover mapping using UAV-derived thermal imagery: limits and opportunities. *Cryos* **17**(3), 1165–1184. doi: 10.5194/tc-17-1165-2023

Haeberli W, Hoelzle M, Paul F and Zemp M (2007) Integrated monitoring of mountain glaciers as key indicators of global climate change: the European Alps. *Annals of Glaciology* **46**, 150–160. doi: 10.3189/172756407782871512

Jol HM (2009) *Ground Penetrating Radar: Theory and Applications*. Amsterdam, Netherlands: Elsevier Sci.

Kääb A, Reynolds JM and Haeberli W (2005) Glacier and permafrost hazards in high mountains. In Huber UM, Bugmann HKM and Reasoner MA (eds), *Global Change and Mountain Regions - An Overview of Current Knowledge*. Dordrecht, Netherlands: Springer, pp. 225–234.

**Kovacs A, Gow AJ and Morey RM** (1995) The in-situ dielectric constant of polar firn revisited. *Cold Regions Science and Technology* **23**(3), 245–256. doi: 10.1016/0165-232X(94)00016-Q

**Li Z, Wang K, Ma H and Wu Y** (2018) An adjusted Inverse Distance Weighted spatial interpolation method. Proc. 3rd Int. Conf. CIMNS, Wuhan, China, 27–28 September 2018, 128–132, doi: 10.2991/cimns-18.2018.29

**Looyenga H** (1965) Dielectric constants of heterogeneous mixtures. *Physicist* **31**(3), 401–406. doi: 10.1016/0031-8914(65)90045-5

**Lundberg A, Richardson-Näslund C and Andersson C** (2006) Snow density variations: consequences for ground-penetrating radar. *Hydrol Process* **20** (7), 1483–1495. doi: 10.1002/hyp.5944

**Marinelli O and Ricci L** (1916) Alcune osservazioni sul ghiacciaio del Gran Sasso. *Riv. Geogr. It* **23**, 399–405.

**Merwade VM, Maidment DR and Goff JA** (2006) Anisotropic considerations while interpolating river channel bathymetry. *Journal of Hydrology* **331**(3–4), 731–741. doi: 10.1016/j.jhydrol.2006.06.018

**Monaco A and Scozzafava M** (2017) A preliminary survey for testing operativity and efficiency of GPR technology by means of unshielded antenna for the study of Calderone Glacier, Central Italy. *Alpine and Mediterranean Quaternary* **30**(1), 5–10.

**Murray T, Booth A and Rippin DM** (2007) Water-content of glacier-ice: limitations on estimates from velocity analysis of surface ground-penetrating radar surveys. *Journal of Environmental & Engineering Geophysics* **12**(1), 87–99. doi: 10.2113/JEEG12.1.87

**Pavoni M and 5 others** (2023) Combining ground penetrating radar and frequency domain electromagnetic surveys to characterize the structure of the Calderone Glacieret (Gran Sasso d'Italia, Italy). *Remote Sensing* **15**(10), 1–17. doi: 10.3390/rs15102615

**Pecci M** (2001) The historical and iconographic research in the reconstruction of the variation of the Calderone Glacier: state of the art and perspective. In Visconti G, Beniston M, Iannorelli ED and Barba D (eds), *Advances in Global Change Research*, Vol. **9**. Dordrecht, Netherlands: Kluwer Acad. Publ., pp. 505–512.

**Pecci M and D'Aquila P** (2011) Geomorphological features and cartography of the Gran Sasso d'Italia massif between Corno Grande-Corno Piccolo and Pizzo Intermesoli. *Geografia Fisica e Dinamica Quaternaria* **34**, 127–143. doi: 10.4461/GFDQ.2011.34.13

**Pecci M, De Sisti G, Marino A and Smiraglia C** (2001) New radar surveys in monitoring the evolution of the Calderone glacier (central Apennines, Italy). *Suppl. Geografia Fisica e Dinamica Quaternaria* **V**, 145–150.

**Pecci M, D'Agata C and Smiraglia C** (2008) Ghiacciaio del Calderone (Apennines, Italy): the mass balance of a shrinking Mediterranean glacier. *Geografia Fisica e Dinamica Quaternaria* **31**, 55–62.

**Pecci M, Cappelletti D, Esposito G, D'Aquila P and Caira T** (2017) Relazioni della campagna glaciologica 2016 - Ghiacciaio del Calderone. *Geografia Fisica e Dinamica Quaternaria* **40**(2), 318–319. doi: 10.4461/GFDQ.2017. 40.14

**Rau F, Mauz F, Vogt S, Khalsa SJS and Raup B** (2005) *Illustrated GLIMS Glacier Classification Manual: Glacier Classification Guidance for the GLIMS Glacier Inventory.* Freiburg, Germany: Ins. Physical Geography.

**Richardson SD and Reynolds JM** (2000) An overview of glacial hazards in the Himalayas. *Quaternary International* **65-66**, 31–47. doi: 10.1016/ S1040-6182(99)00035-X

**Robin GdQ** (1975) Velocity of radio waves in ice by means of a bore-hole interferometric technique. *Journal of Glaciology* **15**(73), 151–160. doi: 10. 3189/S0022143000034341

**Rossini M and 7 others** (2018) Rapid melting dynamics of an alpine glacier with repeated UAV photogrammetry. *Geomorph.*, **304**, 159–172, doi: 10. 1016/j.geomorph.2017.12.039

**Rovelli E** (2006) Il Ghiacciaio del Calderone: Ricostruzione delle oscillazioni recenti mediante l'analisi delle fonti iconografico-storiche e meteoclimatiche (Gran Sasso d'Italia, Abruzzo). *Terra Glacialis* **9**, 9–45.

**Rui XP, Yu XT, Lu J, Ashraf MA and Song XF** (2016) An algorithm for generation of DEMs from contour lines considering geomorphic features. *Earth Sciences Research Journal* **20**(2), G1–G9. doi: 10.15446/esrj.v20n2.55348

**Shukla A, Gupta RP and Arora MK** (2010) Delineation of debris-covered glacier boundaries using optical and thermal remote sensing data. *Remote Sensing Letters* **1**(1), 11–17. doi: 10.1080/01431160903159316

**Smiraglia C and Diolaiuti G** (2015) *The New Italian Glacier Inventory.* Bergamo, Italy: Ev-K2-CNR.

**Wang P, Li Z, Li H, Wang W and Yao H** (2014) Comparison of glaciological and geodetic mass balance at Urumqi Glacier No. 1, Tian Shan, Central Asia. *Global and Planetary Change* **114**, 14–22. doi: 10.1016/j.gloplacha. 2014.01.001

**Winkler S and 5 others** (2010) An introduction to mountain glaciers as climate indicators with spatial and temporal diversity. *Erdkunde* **64**(2), 97–118. doi: 10.3112/erdkunde.2010.02.01

**Ying X and 5 others** (2012) Direct least square fitting of ellipsoids. Proc. IEEE 21st Int. Conf. Pattern Recognit., Tsukuba, Japan, 11–15 November 2012, 3228–3231.

**Zekollari H, Huss M and Farinotti D** (2020) On the imbalance and response time of glaciers in the European Alps. *Geophysical Research Letters* **47**(2), 1–9. doi: 10.1029/2019GL085578

**Zemp M, Hoelzle M and Haeberli W** (2009) Six decades of glacier mass-balance observations: a review of the worldwide monitoring network. *Annals of Glaciology* **50**(50), 101–111. doi: 10.3189/172756409787769591